Layer-dependent magnetism and spin fluctuations in atomically thin van der Waals magnet $CrPS_4$

Mengqi Huang,[1] Jazmine C. Green,[2] Jingcheng Zhou,[1] Violet Williams,[3] Senlei Li,[1] Hanyi Lu,[1] Dziga Djugba,[1] Hailong Wang,[4,5] Benedetta Flebus,[3] Ni Ni,[2] and Chunhui Rita Du[1,4,5,*]

[1]Department of Physics, University of California, San Diego, La Jolla, California 92093, USA
[2]Department of Physics and Astronomy, University of California, Los Angeles, California 90095, USA
[3]Department of Physics, Boston College, Chestnut Hill, Massachusetts 02467, USA
[4]Center for Memory and Recording Research, University of California, San Diego, La Jolla, California 92093, USA
[5]School of Physics, Georgia Institute of Technology, Atlanta, Georgia 30332, USA

*Correspondence to: c1du@physics.ucsd.edu

Keywords: quantum sensing, nitrogen-vacancy magnetometry, magnetic two-dimensional materials, spin fluctuations, tunneling magnetoresistance.

Abstract: van der Waals (vdW) magnets, an emerging family of two-dimensional (2D) materials, have received tremendous attention due to their rich fundamental physics and significant potential for cutting-edge technological applications. In contrast to the conventional bulk counterparts, vdW magnets exhibit significant tunability of local material properties, such as stacking engineered interlayer coupling and layer-number dependent magnetic and electronic interactions, which promise to deliver previously unavailable merits to develop multifunctional microelectronic devices. As a further ingredient of this emerging topic, here we report nanoscale quantum sensing and imaging of atomically thin vdW magnet chromium thiophosphate $CrPS_4$, revealing its characteristic layer-dependent 2D static magnetism and dynamic spin fluctuations. We also show a large tunneling magnetoresistance in $CrPS_4$-based spin filter vdW heterostructures. The excellent material stability, robust strategy against environmental degradation, in combination with tailored magnetic properties highlight the potential of $CrPS_4$ in developing state-of-the-art 2D spintronic devices for next-generation information technologies.

Recent discovery of van der Waals (vdW) magnets has inspired a vast research interest in exploring transformative two-dimensional (2D) spintronic devices capable of delivering novel functionalities, such as ultra-high densities, improved compatibility to device integration, and tailored heterostructure engineering, to next-generation information sciences and technologies.[1,2] To date, CrX_3 (X = I, Cl, Br),[3–9] Fe_3GeTe_2,[10] $Cr_2Ge_2Te_6$,[11] and $MnBi_2Te_4$ $(Bi_2Te_3)_n$ [12,13] have been prominent candidates of this family, which exhibit a range of exotic material properties such as layer-dependent magnetic and electronic interactions,[3,14,15] stacking-induced moiré magnetism,[16–19] and unconventional magnetic tunneling effects [20–22] that are currently under intensive investigation. Despite the enormous technological promise and rich fundamental physics, implementation of 2D spintronic devices incorporating vdW magnets for practical applications remains at its infancy. An apparent challenge arises from the materials' ultrahigh sensitivity to air and light exposure,[11,23] which prohibits a broad range of their applications in the ambient environment.

Recently, the emergence of a more robust magnetic vdW material chromium thiophosphate $CrPS_4$ with improved chemical stability provides an appealing platform to tackle the above challenges, expanding the available material scope for 2D spintronic research.[24–27] Here we report nanoscale quantum sensing and imaging of atomically thin $CrPS_4$ crystals. Taking advantage of nitrogen-vacancy (NV) nanomagnetometry techniques,[28–32] we investigate layer-dependent (anti)ferromagnetism and spin fluctuations in $CrPS_4$ nanoflakes. Notably, robust spin fluctuations are observed in both odd and even layer $CrPS_4$ nanoflakes and the obtained magnetic susceptibility monotonically increases with reducing layer numbers. We also prepared $CrPS_4$-based vdW spin filter devices and observed a large tunneling magnetoresistance up to 100% below the magnetic phase transition temperature. Our results highlight the significant potential of $CrPS_4$ for developing robust, air-stable vdW spin logic devices for practical applications. The demonstrated NV quantum metrology techniques could be readily applied to a broad family of vdW crystals, opening a new avenue for probing the spin-related phenomena in emergent quantum states of matter.

We first briefly review the crystal structure and magnetic properties of the vdW material in the current study. $CrPS_4$ has a monoclinic crystal symmetry where each Cr atom is surrounded by six S atoms forming a slightly distorted octahedron CrS_6 in a 2D rectangular lattice as shown in Fig. 1a.[24,25] The one-dimensional chains of the chromium octahedra arranged along the *a*-axis are interconnected by P atoms. Below the Néel temperature of 38 K,[26] $CrPS_4$ bulk behaves as a typical A-type antiferromagnet in the magnetic ground state, where magnetic moments carried by Cr^{3+} in individual monolayers align parallel with each other along the *c*-axis direction and any two neighboring magnetic monolayers are antiferromagnetically coupled (Fig. 1a). By applying an external magnetic field B_{ext} along the *c*-axis direction, $CrPS_4$ will be driven to the canted antiferromagnetic phase at spin-flop transition fields around ± 7 kG, and eventually enters the forced ferromagnetic state around 80 kG (Section S1, Supporting Information).[26]

To evaluate the alternating antiferromagnetic and ferromagnetic like behaviors in even and odd layer $CrPS_4$ crystals, we utilize NV wide-field magnetometry techniques [28–31] to image spatially resolved static magnetization and spin fluctuations at the nanoscale. An NV center consists of a nitrogen atom adjacent to a carbon atom vacancy in one of the nearest neighboring sites of a diamond crystal lattice.[32,33] The negatively charged NV state has an $S = 1$ electron spin

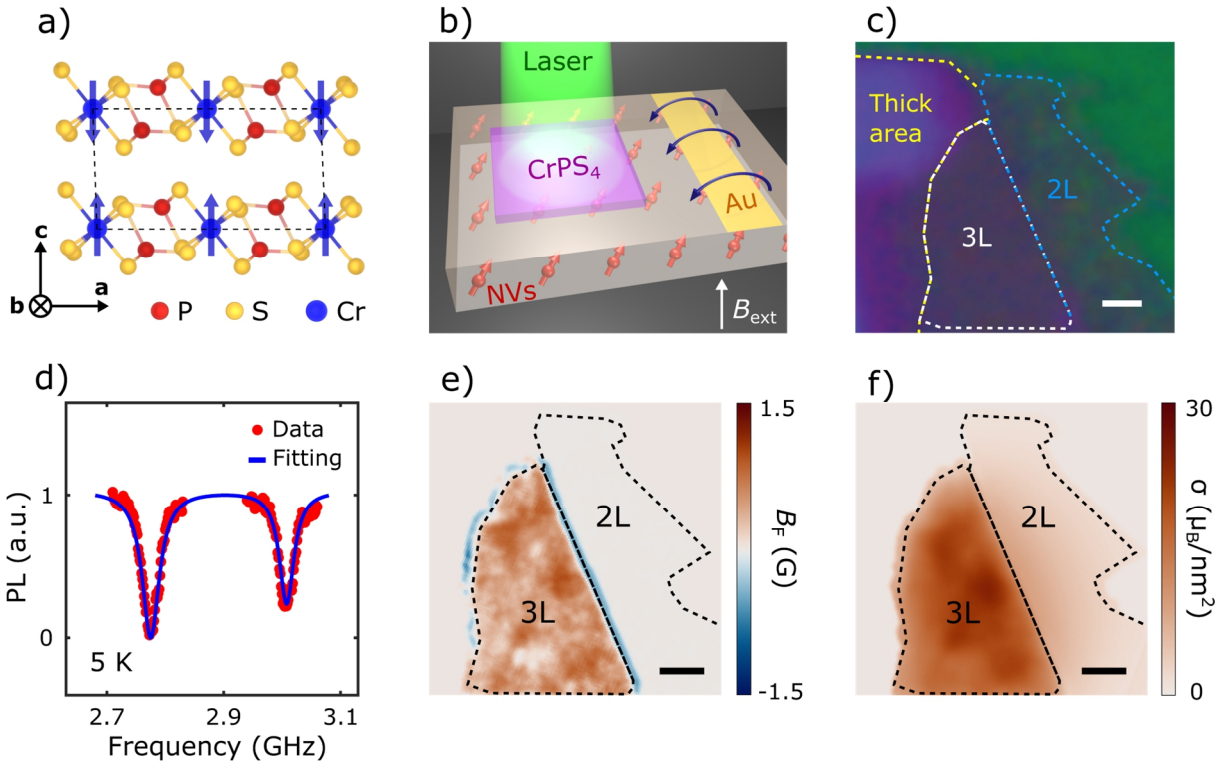

Figure 1. Quantum sensing of atomically thin $CrPS_4$ using NV wide-field magnetometry techniques. a) Crystal and magnetic structures of $CrPS_4$. The blue, yellow, and red balls represent Cr, S, and P atoms, respectively. Blue arrows denote local magnetic moments carried by Cr atoms in two neighboring magnetic monolayers of $CrPS_4$. b) Schematic of NV wide-field magnetometry platform in which a $CrPS_4$ nanoflake is transferred onto a diamond substrate containing shallowly implanted NV centers. c) Optical microscope image of an atomically thin $CrPS_4$ crystal with characterized layer numbers for individual sample areas. The crystal is exfoliated onto an oxidized silicon substrate. d) A typical set of optically detected magnetic resonance spectrum showing the Zeeman splitting of NV spin energy levels. e-f) Wide-field imaging of magnetic stray field B_F (e) and reconstructed magnetization σ (f) of the prepared $CrPS_4$ flake at 5 K. The dashed lines outline the boundary of the bilayer and trilayer $CrPS_4$ flakes. The scale bar is 2 μm in Figs. 1c, 1e, and 1f.

and serves as a three-level quantum system for implementing qubit-based nanomagnetometry. Figure 1b shows the schematic of our measurement platform, where a (001)-oriented diamond sample containing shallowly implanted NV ensembles is used for wide-field imaging measurements. Atomically thin $CrPS_4$ flakes were first exfoliated on an oxidized Si substrate as shown by an optical microscope image in Fig. 1c. The layer number of individual sample areas is determined by thickness-dependent optical contrast and confirmed by atomic force microscopy characterizations (Section S1, Supporting Information). Exfoliated $CrPS_4$ flakes were subsequently transferred onto the diamond sample for NV magnetometry measurements which will be discussed in detail below.

We first utilize NV centers to investigate the layer-dependent static magnetization of the $CrPS_4$ sample. d.c. wide-field magnetometry utilizes the Zeeman effect [32,33] of NV ensembles to spatially resolve magnetic stray fields emanating from proximate $CrPS_4$ samples. Figure 1d presents a typical set of NV electron spin resonance (ESR) spectrum recorded at a single camera pixel over the $CrPS_4$ sample at 5 K. In the current work, a small external magnetic field B_{ext} of ~70

G is applied along the out-of-plane (OOP) direction of the sample. NV ensembles in the diamond substrate have four possible spin orientations with a mirror symmetry axis along the OOP direction. Considering the spontaneous perpendicular anisotropy of $CrPS_4$, the measured NV ESR spectrum shows four-fold degeneracy with only one pair of split NV spin energy levels (Fig. 1d), from which the magnitude of the OOP stray field B_F exclusively arising from the $CrPS_4$ sample can be measured (Section S2, Supporting Information).[34] By measuring the field-induced Zeeman splitting at every pixel of the captured image, we are able to obtain a magnetic stray field B_F map of the $CrPS_4$ sample as shown in Fig. 1e. Notably, magnetic stray field predominantly emerges from the trilayer $CrPS_4$ flake area while B_F arising from the bilayer $CrPS_4$ exhibits a vanishingly small value. The observed strong even-odd contrast is attributed to the layer-number determined (un)compensated magnetization of atomically thin $CrPS_4$ crystals. In the presented NV wide-field magnetometry measurement platform, the vertical distance between NV spin sensors and the sample surface is ~10 nm, much larger than the thickness of $CrPS_4$ flakes. Thus, magnetic stray fields generated by individual ferromagnetic monolayers of an even layer $CrPS_4$ crystal nearly compensate at the NV sites while an odd layer $CrPS_4$ sample could produce a significantly pronounced stray field due to the uncompensated net magnetization. Note that the sign of the measured stray field reverses across the boundary of the odd layer $CrPS_4$ flake owing to the characteristic dipole nature. Through established reverse-propagation protocols,[7,16] spatially resolved magnetization patterns of the $CrPS_4$ sample can be reconstructed from the stray field image as presented in Fig. 1f. The trilayer $CrPS_4$ flake shows robust magnetization with a spatially averaged value of ~20 μ_B/nm^2, in qualitative agreement with results reported in previous studies.[26] It is instructive to note that the observed spatial variations of local $CrPS_4$ magnetization could result from inhomogeneities, magnetic domains, and defects.[25]

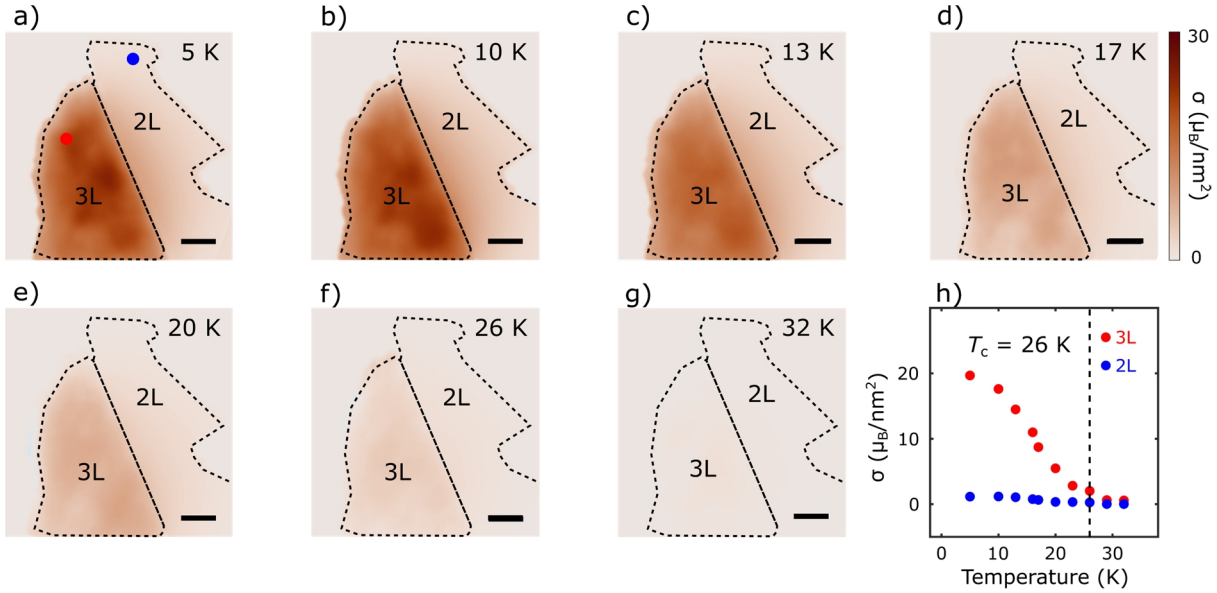

Figure 2. Temperature dependent magnetization maps of a $CrPS_4$ flake probed by NV magnetometry. a-g) Magnetization maps of the prepared $CrPS_4$ nanoflakes measured with a perpendicular magnetic field B_{ext} = 70 G at temperatures of 5 K (a), 10 K (b), 13 K (c), 17 K (d), 20 K (e), 26 K (f), and 32 K (g), respectively. The black dashed lines outline the boundary of the bilayer and trilayer $CrPS_4$ flakes of interest, and the scale bar is 2 μm. h) Temperature dependence of magnetization measured at two local sample sites of the bilayer and trilayer $CrPS_4$ flakes.

To investigate the second-order magnetic phase transition of the sample, we performed systematic NV wide-field magnetometry measurements to visualize the evolution of the static $CrPS_4$ magnetization patterns across the Néel temperature. Figures 2a-2g present the reconstructed magnetization maps of the $CrPS_4$ sample measured from 5 K to 32 K. In the low temperature regime ($T \leq 10$ K), the exfoliated $CrPS_4$ sample exhibits robust magnetization in the trilayer flake area, as shown in Figs. 2a and 2b. The measured uncompensated magnetic moment decreases with increasing temperature due to thermally induced spin fluctuations (Figs. 2c-2e). When approaching the Néel temperature of $CrPS_4$ where the energy scale of thermal spin fluctuations becomes comparable to the intralayer ferromagnetic exchange interaction, long-range magnetic order sustained by the intrinsic magnetocrystalline anisotropy starts to collapse, accompanied by the significant decrease of the $CrPS_4$ magnetization (Fig. 2f). At $T = 32$ K above the Néel temperature, no clear magnetic features are observed over the entire $CrPS_4$ flake area as shown in Fig. 2g. Figure 2h summarizes the temperature dependence of the measured magnetic moment at two local sample sites of the trilayer and bilayer $CrPS_4$ flakes. Clear second-order magnetic phase transition is observed with a Néel temperature of ~26 K for the trilayer crystal (Section S3, Supporting Information).

So far, we have shown the strong even-odd contrast of static magnetization of atomically thin $CrPS_4$ crystals. Next, we use wide-field NV spin relaxometry method [30,35–39] to probe intrinsic spin fluctuations in the 2D vdW magnet of interest. Spin fluctuations in an antiferromagnetically correlated system are driven by its time dependent spin density distribution, for example, due to the dynamic imbalance in the thermal occupation of the magnon bands with opposite chiralities.[30] While a fully compensated antiferromagnet exhibits zero net static magnetization, the spin-spin correlation-induced time dependent fluctuations of the average spin density do not vanish.[30] As qubit-based magnetometers, NV centers with excellent quantum coherence are ideally posed to investigate local spin fluctuations in vdW $CrPS_4$ nanoflakes that are challenging to access by conventional magnetometry techniques. The NV spin relaxometry measurements take advantage of the dipole-dipole interaction between spin fluctuations in a magnetic sample and proximal NV centers. Emanating fluctuating magnetic fields at the NV ESR frequencies will accelerate NV spin transitions from the $m_s = 0$ to $m_s = \pm 1$ states, leading to enhancement of the corresponding NV spin relaxation rates [30,40] (Section S2, Supporting Information). By measuring the spin-dependent NV photoluminescence, the occupation probabilities of NV spin states can be quantitatively obtained, allowing for extraction of the NV spin relaxation rate which is proportional to the magnitude of the local fluctuating magnetic fields transverse to the NV axis.

Figures 3a-3f present a series of spin fluctuation induced NV spin relaxation rate Γ_M maps of the $CrPS_4$ sample measured at temperatures from 13 K to 44 K. It is evident that robust magnetic fluctuations with a strong temperature dependence are observed in both bilayer and trilayer $CrPS_4$ crystals as expected from the time dependent spin-spin correlations of the (un)compensated magnetic density.[30,40] To further reveal the layer-number dependent spin fluctuations, Fig. 3g summarizes temperature dependence of spatially averaged NV spin relaxation rates for $CrPS_4$ crystals with different layer numbers. Note that the tetralayer and six-layer $CrPS_4$ samples were separately prepared on other diamond substrates for NV measurements (Section S3, Supporting Information). One can see that the measured NV spin relaxation rates consistently show an

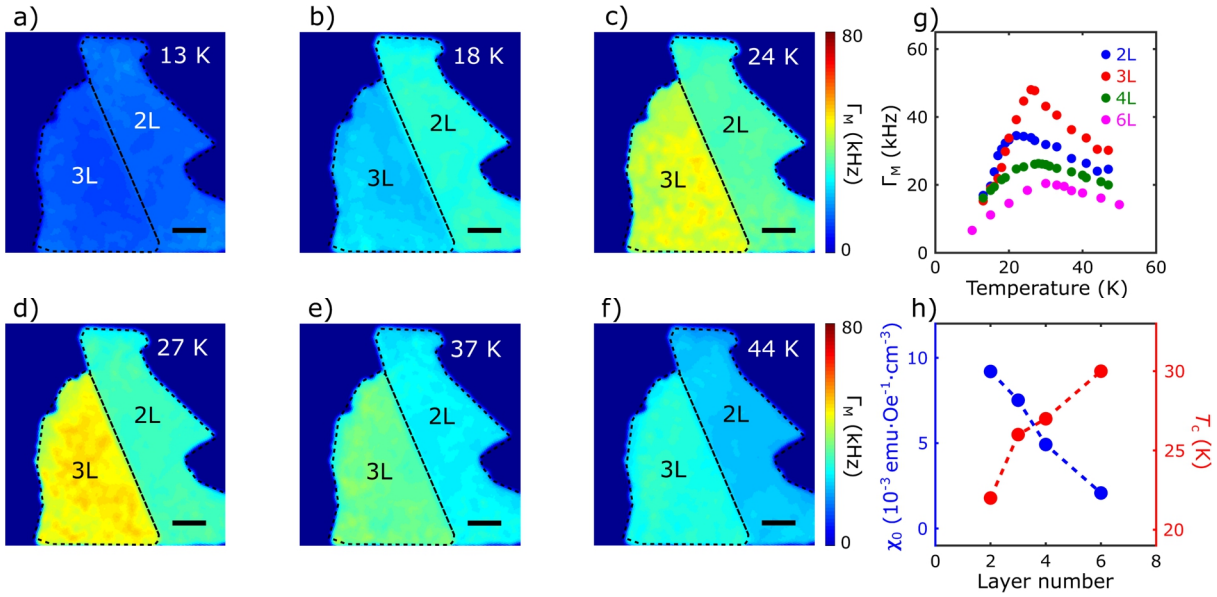

Figure 3. Quantum imaging of spin fluctuations in an atomically thin $CrPS_4$ flake. a-f) NV spin relaxation maps of the prepared bilayer and trilayer $CrPS_4$ flakes measured at temperatures of 13 K (a), 18 K (b), 24 K (c), 27 K (d), 37 K (e), and 44 K (f), respectively. The NV ESR frequency is set to be 2.78 GHz in these measurements with an external perpendicular magnetic field B_{ext} of 70 G. The dashed lines outline the boundary of the bilayer and trilayer $CrPS_4$ flakes of interest, and the scale bar is 2 μm. g) Temperature dependence of spatially averaged NV spin relaxation rate Γ_M for bilayer, trilayer, tetralayer, and sixlayer $CrPS_4$ crystals, showing peak values around the corresponding magnetic phase transition temperatures. h) Layer number dependence of magnetic critical temperature T_c and longitudinal magnetic susceptibility χ_0 of atomically thin $CrPS_4$ crystals measured at 20 K.

enhancement around the magnetic phase transition of $CrPS_4$ nanoflakes, which is attributed to the divergent magnetic susceptibility χ_0 around the quantum phase transition point.[24] When T is above 30 K, moderate spin fluctuations remain present in $CrPS_4$ due to the finite spin-spin correlations in the paramagnetic state.[41] The obtained Néel temperatures of individual $CrPS_4$ nanoflakes qualitatively increases with the layer number as shown in Fig. 3h, in agreement with previous studies on vdW magnets [10,11]. Fundamentally, the measured NV spin relaxation is mainly driven by the longitudinal spin fluctuations of $CrPS_4$, which is directly related to the static longitudinal magnetic susceptibility χ_0 of the sample.[30,40,42] By invoking a theoretical model developed in Ref. 30, longitudinal magnetic susceptibility of atomically thin $CrPS_4$ crystals can be quantitatively measured as presented in Fig. 3h (Section S4, Supporting Information). When $T = 20$ K, χ_0 of six-layer $CrPS_4$ is estimated to be 2.3×10^{-3} emu·Oe^{-1}·cm^{-3}. As the layer number decreases, magnetic order of $CrPS_4$ crystals becomes less robust and more vulnerable to external perturbations, resulting in a significantly enhanced magnetic susceptibility. It is worth mentioning that the NV spin relaxation rate measured around Néel temperatures first increases with the layer-number of the vdW crystals, reaching a peak value for trilayer $CrPS_4$. Further increase of the sample thickness results in significant decay of Γ_M. The observed experimental feature can be explained by the two competing factors on the measured NV spin relaxation rates: sample thickness and intrinsic magnetic susceptibility χ_0 of $CrPS_4$ crystals. In the low thickness regime ($\lesssim 3$ layer), sample thickness is the dominant factor that determines the magnitude of spin fluctuations in $CrPS_4$ while

magnetic susceptibility plays a more prominent role in the large sample thickness regime (> 3 layer).

In comparison with conventional vdW magnets, a distinct advantage of $CrPS_4$ results from its robust material stability against air exposure, providing an attractive platform for developing practical spintronic applications.[24,25] Next, we report our initial efforts along this direction by showing a large tunneling magnetoresistance in $CrPS_4$-based vdW heterostructures. Figure 4a illustrates the device structure for electrical transport measurements, in which an atomically thin

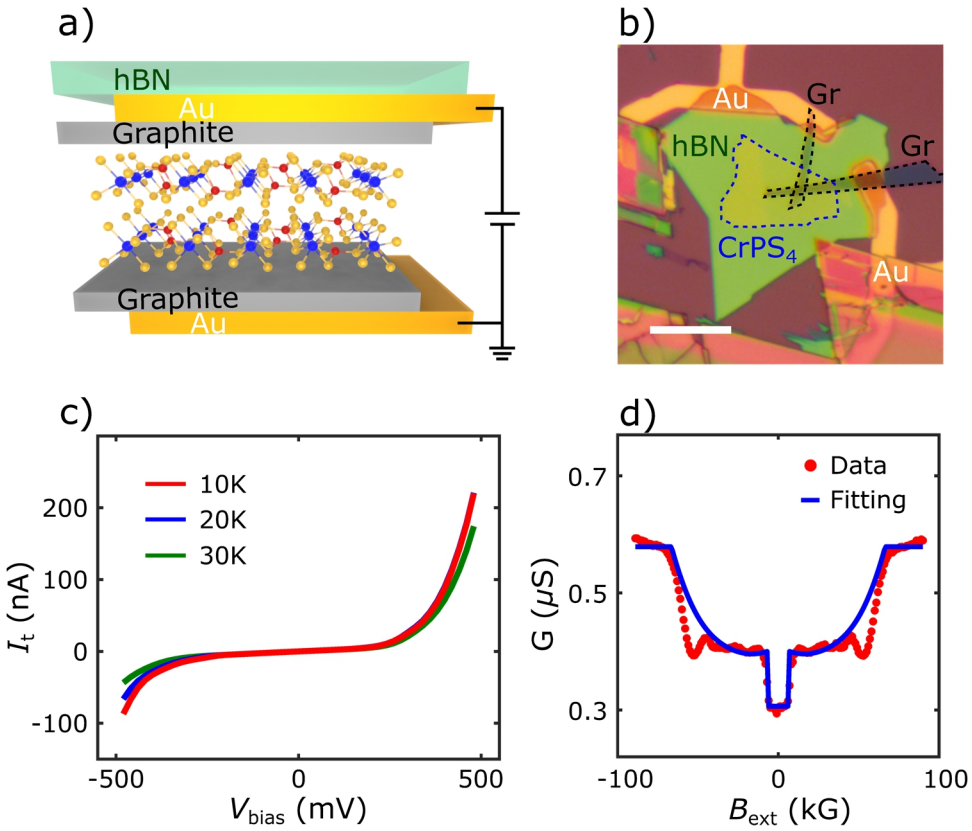

Figure 4. Tunneling magnetoresistance measured in a $CrPS_4$-based vdW junction device. a) Schematic of a vdW spin-filter tunnel junction device consisting of an atomically thin $CrPS_4$ layer sandwiched by two graphite electrodes. b) Optical microscope image of a prepared $CrPS_4$-based vdW tunnel junction device. The blue and black dashed lines outline the boundaries of the tetralayer $CrPS_4$ and graphite flakes, respectively, and the scale bar is 20 μm. c) d.c. bias voltage dependence of the tunneling current of a $CrPS_4$-based vdW junction device measured at 10 K, 20 K, and 30 K in absence of an external magnetic field. d) Tunneling conductance G as a function of an out-of-plane magnetic field B_{ext}, in qualitative agreement with a theoretical model. The experimental results were measured at 10 K with application of a d.c. bias voltage of 300 mV.

$CrPS_4$ layer acts as a spin-filter tunnel barrier sandwiched by graphite electrical contacts. Figure 4b shows an optical microscope image of a prepared tunnel junction device, where blue and black dashed lines outline the boundaries of the tetralayer $CrPS_4$ and graphite flakes, respectively (Section S1, Supporting Information). Considering the overlap between the top and bottom graphite electrodes, the effective tunnel junction area is estimated to be ~4 μm^2. Figure 4c plots the characteristic nonlinear dependence of tunneling current (I_t) on the applied d.c. bias voltage

(V_{bias}). For the atomically thin $CrPS_4$ tunnel layer used in the current study, each magnetic monolayer acts as an independent spin filter that is oppositely aligned in series. The double spin-filtering effect-induced tunneling magnetoresistance arises when the magnetizations of neighboring $CrPS_4$ monolayers are switched from an antiparallel to parallel state. Figure 4d shows the tunneling electrical conductance G as a function of the applied perpendicular magnetic field B_{ext} at 10 K with a d.c. bias voltage of 300 mV. In the low field regime ($B_{ext} \leq 4$ kG), the tetralayer $CrPS_4$ stays in the antiferromagnetic ground state, showing a relatively small G. When B_{ext} exceeds ~ 7 kG, field-induced spin-flop transition drives $CrPS_4$ to the canted antiferromagnetic phase accompanied by a sudden jump of the tunneling conductance. Further increasing B_{ext}, the measured tunneling conductance gradually saturates to a plateau value as $CrPS_4$ evolves to the fully aligned ferromagnetic state at ~80 kG. We have proposed a theoretical model to rationalize the observed spin-dependent electronic tunneling effect in tetralayer $CrPS_4$ (Fig. 4d) (Section S5, Supporting Information). The tunneling magnetoresistance defined as $(G_p - G_{ap})/G_{ap}$ reaches ~100 %, where G_{ap} and G_p are the tunneling conductance of the junction device in the antiferromagnetic and ferromagnetic states of $CrPS_4$, respectively.

In summary, we have demonstrated NV wide-field imaging of layer dependent static magnetization and dynamic spin fluctuations in atomically thin $CrPS_4$ crystals. By fabricating $CrPS_4$-based vdW junction devices, we further report a large tunneling magnetoresistance, which is fundamentally related to different magnetic states of the tetralayer $CrPS_4$ tunneling layer. The observed prominent magneto-tunneling effect, the field controllable magnetic orders, together with the robust chemical stability make $CrPS_4$ a promising material candidate to develop functional 2D spintronic devices for practical applications. Our results also highlight the potential of NV centers in probing nanoscale spin related phenomena in low-dimensional vdW materials, opening the possibility of engineering NV-vdW-magnet-based hybrid quantum systems [43] for developing next-generation information technologies.

Methods

Sample and device information. $CrPS_4$ crystals used in the current study were grown by the chemical vapor transport method.[24,44] $CrPS_4$-based spin filter vdW junction devices were prepared using the standard polymer-stamping techniques.[21,45] Selected hexagonal boron nitride (hBN), graphite, $CrPS_4$, and graphite flakes were picked up in order, and the formed vdW stack was then released onto a Si/SiO_2 substrate with pre-patterned Au electrodes. Thanks to the robust chemical stability of $CrPS_4$ crystals, the whole device preparation processes involving handling $CrPS_4$ nanoflakes were performed in the ambient environment.

NV wide-field magnetometry measurements. Single crystal diamond substrates containing shallowly implanted NV centers used in this work are commercially available from the company Qnami.[46] Pulsed NV electron spin resonance (ESR) and spin relaxometry measurements were performed using a custom-designed wide-field microscope. The prepared $CrPS_4$/diamond samples were positioned inside a closed-cycle optical cryostat allowing for NV measurements from 4.5 K to 350 K. Green laser pulses used for NV spin initialization and readout were generated by an electrically driven 515-nm laser. The laser beam spot width after passing the objective was about 20 μm × 20 μm, and was subsequently focused on the diamond surface. NV fluorescence was imaged using a CMOS camera.[46] Pulses to drive the green laser and to trigger the camera exposure were generated by a programmable pulse generator. Continuous microwave currents were generated using Rohde & Schwarz SGS100a and/or Rohde & Schwarz SMB100a signal generators.

Microwave current pulses were generated by sending continuous microwave currents to a microwave switch (Minicircuits ZASWA-2-50DR+) electrically controlled by a programmable pulse generator. The microwave pulses were sent through a microwave combiner (Mini-Circuits ZB3PD-63-S+) and amplified by +50 dB (Mini-Circuits ZHL-25W-63+) before being delivered to the on-chip Au stripline patterned on diamond samples. The external magnetic field applied in our NV measurements was generated by a cylindrical NdFeB permanent magnet attached to a scanning stage inside the optical cryostat.

Supporting Information. The Supporting Information is available free of charge via the internet at http://pubs.acs.org. Details on Material and device information; NV wide-field magnetometry measurements; Extended NV wide-field imaging results; Inferring longitudinal magnetic susceptibility from NV spin relaxometry measurements; Theoretical model of field-dependent magnetic tunneling conductance of atomically thin $CrPS_4$.

Author contributions: M.H. performed the NV measurements and analyzed the data with H. L and H. W. J. Z., S. L., and D. D. prepared the devices. S. L. performed the electrical transport measurements. J. G. and N. N. provided $CrPS_4$ bulk crystals. V. W. and B. F. provided theoretical input on the tunneling magnetoresistance measured in $CrPS_4$-based spin filter vdW heterostructures. C. R. D. supervised the project.

Notes: The authors declare no financial interest.

Acknowledgements: M. H., H. L., H. W., and C. R. D. were supported by the Air Force Office of Scientific Research under award No. FA9550-20-1-0319 and its Young Investigator Program under award No. FA9550-21-1-0125. J. Z. and D. D. acknowledged the support from U. S. National Science Foundation (NSF) under award No. DMR-2046227. S. L. acknowledged the support from U.S. Department of Energy (DOE), Office of Science, Basic Energy Sciences (BES), under award No. DE-SC0022946. Work at UCLA was supported by DOE, Office of Science, Office of Basic Energy Sciences under Award No. DE-SC0021117. B. F. was supported by the NSF under Grant No. NSF DMR-2144086.

References:

(1) Sierra, J. F.; Fabian, J.; Kawakami, R. K.; Roche, S.; Valenzuela, S. O. Van Der Waals Heterostructures for Spintronics and Opto-Spintronics. *Nat. Nanotechnol.* **2021**, *16* (8), 856–868.

(2) Burch, K. S.; Mandrus, D.; Park, J.-G. Magnetism in Two-Dimensional van Der Waals Materials. *Nature* **2018**, *563* (7729), 47–52.

(3) Huang, B.; Clark, G.; Navarro-Moratalla, E.; Klein, D. R.; Cheng, R.; Seyler, K. L.; Zhong, D.; Schmidgall, E.; McGuire, M. A.; Cobden, D. H.; Yao, W.; Xiao, D.; Jarillo-Herrero, P.; Xu, X. Layer-Dependent Ferromagnetism in a van Der Waals Crystal down to the Monolayer Limit. *Nature* **2017**, *546* (7657), 270–273.

(4) Jin, W.; Ye, Z.; Luo, X.; Yang, B.; Ye, G.; Yin, F.; Kim, H. H.; Rojas, L.; Tian, S.; Fu, Y.; Yan, S.; Lei, H.; Sun, K.; Tsen, A. W.; He, R.; Zhao, L. Tunable Layered-Magnetism–Assisted Magneto-Raman Effect in a Two-Dimensional Magnet CrI_3. *Proc. Natl. Acad. Sci. U.S.A.* **2020**, *117* (40), 24664–24669.

(5) McGuire, M. A.; Clark, G.; Kc, S.; Chance, W. M.; Jellison, G. E.; Cooper, V. R.; Xu, X.; Sales, B. C. Magnetic Behavior and Spin-Lattice Coupling in Cleavable van Der Waals Layered $CrCl_3$ Crystals. *Phys. Rev. Mater.* **2017**, *1* (1), 014001.

(6) MacNeill, D.; Hou, J. T.; Klein, D. R.; Zhang, P.; Jarillo-Herrero, P.; Liu, L. Gigahertz Frequency Antiferromagnetic Resonance and Strong Magnon-Magnon Coupling in the Layered Crystal $CrCl_3$. *Phys. Rev. Lett.* **2019**, *123* (4), 047204.

(7) Thiel, L.; Wang, Z.; Tschudin, M. A.; Rohner, D.; Gutiérrez-Lezama, I.; Ubrig, N.; Gibertini, M.; Giannini, E.; Morpurgo, A. F.; Maletinsky, P. Probing Magnetism in 2D Materials at the Nanoscale with Single-Spin Microscopy. *Science* **2019**, *364* (6444), 973–976.

(8) Sun, Q.-C.; Song, T.; Anderson, E.; Brunner, A.; Förster, J.; Shalomayeva, T.; Taniguchi, T.; Watanabe, K.; Gräfe, J.; Stöhr, R.; Xu, X.; Wrachtrup, J. Magnetic Domains and Domain Wall Pinning in Atomically Thin $CrBr_3$ Revealed by Nanoscale Imaging. *Nat. Commun.* **2021**, *12* (1), 1989.

(9) Zhang, X.-Y.; Wang, Y.-X.; Tartaglia, T. A.; Ding, T.; Gray, M. J.; Burch, K. S.; Tafti, F.; Zhou, B. B. Ac Susceptometry of 2D van Der Waals Magnets Enabled by the Coherent Control of Quantum Sensors. *PRX Quantum* **2021**, *2* (3), 030352.

(10) Deng, Y.; Yu, Y.; Song, Y.; Zhang, J.; Wang, N. Z.; Sun, Z.; Yi, Y.; Wu, Y. Z.; Wu, S.; Zhu, J.; Wang, J.; Chen, X. H.; Zhang, Y. Gate-Tunable Room-Temperature Ferromagnetism in Two-Dimensional Fe_3GeTe_2. *Nature* **2018**, *563* (7729), 94–99.

(11) Gong, C.; Li, L.; Li, Z.; Ji, H.; Stern, A.; Xia, Y.; Cao, T.; Bao, W.; Wang, C.; Wang, Y.; Qiu, Z. Q.; Cava, R. J.; Louie, S. G.; Xia, J.; Zhang, X. Discovery of Intrinsic Ferromagnetism in Two-Dimensional van Der Waals Crystals. *Nature* **2017**, *546* (7657), 265–269.

(12) Deng, Y.; Yu, Y.; Shi, M. Z.; Guo, Z.; Xu, Z.; Wang, J.; Chen, X. H.; Zhang, Y. Quantum Anomalous Hall Effect in Intrinsic Magnetic Topological Insulator $MnBi_2Te_4$. *Science* **2020**, *367* (6480), 895–900.

(13) Hu, C.; Ding, L.; Gordon, K. N.; Ghosh, B.; Tien, H.-J.; Li, H.; Linn, A. G.; Lien, S.-W.; Huang, C.-Y.; Mackey, S.; Liu, J.; Reddy, P. V. S.; Singh, B.; Agarwal, A.; Bansil, A.; Song, M.; Li, D.; Xu, S.-Y.; Lin, H.; Cao, H.; Chang, T.-R.; Dessau, D.; Ni, N. Realization of an Intrinsic Ferromagnetic Topological State in $MnBi_8Te_{13}$. *Sci. Adv.* **2020**, *6* (30), eaba4275.

(14) Yang, S.; Xu, X.; Zhu, Y.; Niu, R.; Xu, C.; Peng, Y.; Cheng, X.; Jia, X.; Huang, Y.; Xu, X.; Lu, J.; Ye, Y. Odd-Even Layer-Number Effect and Layer-Dependent Magnetic Phase Diagrams in $MnBi_2Te_4$. *Phys. Rev. X* **2021**, *11* (1), 011003.

(15) Gao, A.; Liu, Y.-F.; Hu, C.; Qiu, J.-X.; Tzschaschel, C.; Ghosh, B.; Ho, S.-C.; Bérubé, D.; Chen, R.; Sun, H.; Zhang, Z.; Zhang, X.-Y.; Wang, Y.-X.; Wang, N.; Huang, Z.; Felser, C.; Agarwal, A.; Ding, T.; Tien, H.-J.; Akey, A.; Gardener, J.; Singh, B.; Watanabe, K.; Taniguchi, T.; Burch, K. S.; Bell, D. C.; Zhou, B. B.; Gao, W.; Lu, H.-Z.; Bansil, A.; Lin, H.; Chang, T.-R.; Fu, L.; Ma, Q.; Ni, N.; Xu, S.-Y. Layer Hall Effect in a 2D Topological Axion Antiferromagnet. *Nature* **2021**, *595* (7868), 521–525.

(16) Song, T.; Sun, Q.-C.; Anderson, E.; Wang, C.; Qian, J.; Taniguchi, T.; Watanabe, K.; McGuire, M. A.; Stöhr, R.; Xiao, D.; Cao, T.; Wrachtrup, J.; Xu, X. Direct Visualization of Magnetic Domains and Moiré Magnetism in Twisted 2D Magnets. *Science* **2021**, *374* (6571), 1140–1144.

(17) Xu, Y.; Ray, A.; Shao, Y.-T.; Jiang, S.; Lee, K.; Weber, D.; Goldberger, J. E.; Watanabe, K.; Taniguchi, T.; Muller, D. A.; Mak, K. F.; Shan, J. Coexisting Ferromagnetic–Antiferromagnetic State in Twisted Bilayer CrI_3. *Nat. Nanotechnol.* **2021**, *17* (2),143-147.

(18) Xie, H.; Luo, X.; Ye, G.; Ye, Z.; Ge, H.; Sung, S. H.; Rennich, E.; Yan, S.; Fu, Y.; Tian, S.; Lei, H.; Hovden, R.; Sun, K.; He, R.; Zhao, L. Twist Engineering of the Two-Dimensional Magnetism in Double Bilayer Chromium Triiodide Homostructures. *Nat. Phys.* **2021**, *18* (1), 30-36.

(19) Cheng, G.; Rahman, M. M.; Allcca, A. L.; Rustagi, A.; Liu, X.; Liu, L.; Fu, L.; Zhu, Y.; Mao, Z.; Watanabe, K.; Taniguchi, T.; Upadhyaya, P.; Chen, Y. P. Electrically Tunable Moiré Magnetism in Twisted Double Bilayers of Chromium Triiodide. *Nat Electron* **2023**, *6* (6), 434–442.

(20) Klein, D. R.; MacNeill, D.; Lado, J. L.; Soriano, D.; Navarro-Moratalla, E.; Watanabe, K.; Taniguchi, T.; Manni, S.; Canfield, P.; Fernández-Rossier, J.; Jarillo-Herrero, P. Probing Magnetism in 2D van Der Waals Crystalline Insulators via Electron Tunneling. *Science* **2018**, *360* (6394), 1218–1222.

(21) Song, T.; Cai, X.; Tu, M. W.-Y.; Zhang, X.; Huang, B.; Wilson, N. P.; Seyler, K. L.; Zhu, L.; Taniguchi, T.; Watanabe, K.; McGuire, M. A.; Cobden, D. H.; Xiao, D.; Yao, W.; Xu, X. Giant Tunneling Magnetoresistance in Spin-Filter van Der Waals Heterostructures. *Science* **2018**, *360* (6394), 1214–1218.

(22) Wang, Z.; Gutiérrez-Lezama, I.; Ubrig, N.; Kroner, M.; Gibertini, M.; Taniguchi, T.; Watanabe, K.; Imamoğlu, A.; Giannini, E.; Morpurgo, A. F. Very Large Tunneling Magnetoresistance in Layered Magnetic Semiconductor CrI_3. *Nat. Commun.* **2018**, *9* (1), 2516.

(23) Shcherbakov, D.; Stepanov, P.; Weber, D.; Wang, Y.; Hu, J.; Zhu, Y.; Watanabe, K.; Taniguchi, T.; Mao, Z.; Windl, W.; Goldberger, J.; Bockrath, M.; Lau, C. N. Raman Spectroscopy, Photocatalytic Degradation, and Stabilization of Atomically Thin Chromium Tri-Iodide. *Nano Lett.* **2018**, *18* (7), 4214–4219.

(24) Son, J.; Son, S.; Park, P.; Kim, M.; Tao, Z.; Oh, J.; Lee, T.; Lee, S.; Kim, J.; Zhang, K.; Cho, K.; Kamiyama, T.; Lee, J. H.; Mak, K. F.; Shan, J.; Kim, M.; Park, J.-G.; Lee, J. Air-Stable and Layer-Dependent Ferromagnetism in Atomically Thin van Der Waals $CrPS_4$. *ACS Nano* **2021**, *15* (10), 16904–16912.

(25) Lee, J.; Ko, T. Y.; Kim, J. H.; Bark, H.; Kang, B.; Jung, S.-G.; Park, T.; Lee, Z.; Ryu, S.; Lee, C. Structural and Optical Properties of Single- and Few-Layer Magnetic Semiconductor $CrPS_4$. *ACS Nano* **2017**, *11* (11), 10935–10944.

(26) Peng, Y.; Ding, S.; Cheng, M.; Hu, Q.; Yang, J.; Wang, F.; Xue, M.; Liu, Z.; Lin, Z.; Avdeev, M.; Hou, Y.; Yang, W.; Zheng, Y.; Yang, J. Magnetic Structure and Metamagnetic

Transitions in the van Der Waals Antiferromagnet $CrPS_4$. *Adv. Mater.* **2020**, *32* (28), 2001200.
(27) Wu, R.; Ross, A.; Ding, S.; Peng, Y.; He, F.; Ren, Y.; Lebrun, R.; Wu, Y.; Wang, Z.; Yang, J.; Brataas, A.; Kläui, M. Magnetotransport Study of van Der Waals $CrPS_4$/(Pt, Pd) Heterostructures: Spin-Flop Transition and Room-Temperature Anomalous Hall Effect. *Phys. Rev. Appl.* **2022**, *17* (6), 064038.
(28) Tetienne, J.-P.; Dontschuk, N.; Broadway, D. A.; Stacey, A.; Simpson, D. A.; Hollenberg, L. C. L. Quantum Imaging of Current Flow in Graphene. *Sci. Adv.* **2017**, *3* (4), e1602429.
(29) Lenz, T.; Chatzidrosos, G.; Wang, Z.; Bougas, L.; Dumeige, Y.; Wickenbrock, A.; Kerber, N.; Zázvorka, J.; Kammerbauer, F.; Kläui, M.; Kazi, Z.; Fu, K.-M. C.; Itoh, K. M.; Watanabe, H.; Budker, D. Imaging Topological Spin Structures Using Light-Polarization and Magnetic Microscopy. *Phys. Rev. Appl.* **2021**, *15* (2), 024040.
(30) McLaughlin, N. J.; Hu, C.; Huang, M.; Zhang, S.; Lu, H.; Yan, G. Q.; Wang, H.; Tserkovnyak, Y.; Ni, N.; Du, C. R. Quantum Imaging of Magnetic Phase Transitions and Spin Fluctuations in Intrinsic Magnetic Topological Nanoflakes. *Nano Lett.* **2022**, *22* (14), 5810–5817.
(31) Ku, M. J. H.; Zhou, T. X.; Li, Q.; Shin, Y. J.; Shi, J. K.; Burch, C.; Anderson, L. E.; Pierce, A. T.; Xie, Y.; Hamo, A.; Vool, U.; Zhang, H.; Casola, F.; Taniguchi, T.; Watanabe, K.; Fogler, M. M.; Kim, P.; Yacoby, A.; Walsworth, R. L. Imaging Viscous Flow of the Dirac Fluid in Graphene. *Nature* **2020**, *583* (7817), 537–541.
(32) Rondin, L.; Tetienne, J.-P.; Hingant, T.; Roch, J.-F.; Maletinsky, P.; Jacques, V. Magnetometry with Nitrogen-Vacancy Defects in Diamond. *Rep. Prog. Phys.* **2014**, *77* (5), 056503.
(33) Degen, C. L.; Reinhard, F.; Cappellaro, P. Quantum Sensing. *Rev. Mod. Phys.* **2017**, *89* (3), 035002.
(34) Chen, H.; Asif, S.; Whalen, M.; Támara-Isaza, J.; Luetke, B.; Wang, Y.; Wang, X.; Ayako, M.; Lamsal, S.; May, A. F.; McGuire, M. A.; Chakraborty, C.; Xiao, J. Q.; Ku, M. J. H. Revealing Room Temperature Ferromagnetism in Exfoliated Fe_5GeTe_2 Flakes with Quantum Magnetic Imaging. *2D Mater.* **2022**, *9* (2), 025017.
(35) Finco, A.; Haykal, A.; Tanos, R.; Fabre, F.; Chouaieb, S.; Akhtar, W.; Robert-Philip, I.; Legrand, W.; Ajejas, F.; Bouzehouane, K.; Reyren, N.; Devolder, T.; Adam, J.-P.; Kim, J.-V.; Cros, V.; Jacques, V. Imaging Non-Collinear Antiferromagnetic Textures via Single Spin Relaxometry. *Nat. Commun.* **2021**, *12* (1), 767.
(36) McCullian, B. A.; Thabt, A. M.; Gray, B. A.; Melendez, A. L.; Wolf, M. S.; Safonov, V. L.; Pelekhov, D. V.; Bhallamudi, V. P.; Page, M. R.; Hammel, P. C. Broadband Multi-Magnon Relaxometry Using a Quantum Spin Sensor for High Frequency Ferromagnetic Dynamics Sensing. *Nat. Commun.* **2020**, *11* (1), 5229.
(37) van der Sar, T.; Casola, F.; Walsworth, R.; Yacoby, A. Nanometre-Scale Probing of Spin Waves Using Single Electron Spins. *Nat. Commun.* **2015**, *6* (1), 7886.
(38) Andersen, T. I.; Dwyer, B. L.; Sanchez-Yamagishi, J. D.; Rodriguez-Nieva, J. F.; Agarwal, K.; Watanabe, K.; Taniguchi, T.; Demler, E. A.; Kim, P.; Park, H.; Lukin, M. D. Electron-Phonon Instability in Graphene Revealed by Global and Local Noise Probes. *Science* **2019**, *364* (6436), 154-157.
(39) Kolkowitz, S.; Safira, A.; High, A. A.; Devlin, R. C.; Choi, S.; Unterreithmeier, Q. P.; Patterson, D.; Zibrov, A. S.; Manucharyan, V. E.; Park, H.; Lukin, M. D. Probing Johnson Noise and Ballistic Transport in Normal Metals with a Single-Spin Qubit. *Science* **2015**, *347* (6226), 1129–1132.

(40) Flebus, B.; Tserkovnyak, Y. Quantum-Impurity Relaxometry of Magnetization Dynamics. *Phys. Rev. Lett.* **2018**, *121* (18), 187204 .
(41) Brown, P. J.; Ziebeck, K. R. A.; Déportes, J.; Givord, D. Magnetic Correlation in Itinerant Magnetic Materials above T_C (Invited). *J. Appl. Phys.* **1984**, *55* (6), 1881–1886.
(42) Wang, H.; Zhang, S.; McLaughlin, N. J.; Flebus, B.; Huang, M.; Xiao, Y.; Liu, C.; Wu, M.; Fullerton, E. E.; Tserkovnyak, Y.; Du, C. R. Noninvasive Measurements of Spin Transport Properties of an Antiferromagnetic Insulator. *Sci. Adv.* **2022**, *8* (1), eabg8562.
(43) Awschalom, D. D.; Du, C. R.; He, R.; Heremans, F. J.; Hoffmann, A.; Hou, J.; Kurebayashi, H.; Li, Y.; Liu, L.; Novosad, V.; Sklenar, J.; Sullivan, S. E.; Sun, D.; Tang, H.; Tyberkevych, V.; Trevillian, C.; Tsen, A. W.; Weiss, L. R.; Zhang, W.; Zhang, X.; Zhao, L.; Zollitsch, Ch. W. Quantum Engineering With Hybrid Magnonic Systems and Materials (Invited Paper). *IEEE Transactions on Quantum Engineering* **2021**, *2*, 1–36.
(44) Hu, C.; Gao, A.; Berggren, B. S.; Li, H.; Kurleto, R.; Narayan, D.; Zeljkovic, I.; Dessau, D.; Xu, S.; Ni, N. Growth, Characterization, and Chern Insulator State in $MnBi_2Te_4$ via the Chemical Vapor Transport Method. *Phys. Rev. Mater.* **2021**, *5* (12), 124206.
(45) Purdie, D. G.; Pugno, N. M.; Taniguchi, T.; Watanabe, K.; Ferrari, A. C.; Lombardo, A. Cleaning Interfaces in Layered Materials Heterostructures. *Nat. Commun.* **2018**, *9* (1), 5387.
(46) McLaughlin, N. J.; Wang, H.; Huang, M.; Lee-Wong, E.; Hu, L.; Lu, H.; Yan, G. Q.; Gu, G.; Wu, C.; You, Y.-Z.; Du, C. R. Strong Correlation Between Superconductivity and Ferromagnetism in an Fe-Chalcogenide Superconductor. *Nano Lett.* **2021**, *21* (17), 7277–7283.